

Three-dimensional dynamical evolution of cloud particle microphysics in sub-stellar atmospheres

I. Description and exploring Y-dwarf atmospheric variability

Elsbeth K.H. Lee¹ and Kazumasa Ohno²

¹Center for Space and Habitability, University of Bern, Gesellschaftsstrasse 6, CH-3012 Bern, Switzerland

²Division of Science, National Astronomical Observatory of Japan, 2-21-1 Osawa, Mitaka-shi, Tokyo, Japan

Received MM. DD, YY; accepted MM. DD, YY

ABSTRACT

Context. Understanding of cloud microphysics and the evolution of cloud structures in sub-stellar atmospheres remains a key challenge in the JWST era. The abundance of new JWST data necessitates models that are suitable for coupling with large-scale simulations, such as general circulation models (GCMs), in order to fully understand and assess the complex feedback effects of clouds on the atmosphere, and their influence on observed spectral and variability characteristics.

Aims. We aim to develop a 2-moment, time-dependent bulk microphysical cloud model that is suitable for GCMs of sub-stellar atmospheres.

Methods. We derive a set of moment equations for the particle mass distribution and develop a microphysical cloud model employing a 2-moment approach. We include homogeneous nucleation, condensation, and collisional microphysical processes that evolve the moments of a particle size distribution in time. We couple our new 2-moment scheme with the Exo-FMS GCM to simulate the evolution of KCl clouds in a $T_{\text{int}} = 400$ K, $\log g = 4.25$ Y-dwarf atmosphere and examine the effect of cloud opacity on the atmospheric characteristics.

Results. Our results show a generally homogeneous global KCl cloud, with only slight variations occurring in the equatorial regions. The atmosphere is generally sluggish and stagnant, with near-zero vertical velocities throughout most of the atmosphere. Only very small grains $\sim 0.01 \mu\text{m}$ remain lofted in the atmosphere. Our results conform with dynamical theories for this parameter regime, with our model showing minimal ($\sim 0.2\%$) spectral variability at mid-infrared wavelengths.

Conclusions. Our study demonstrates that the 2-moment bulk cloud microphysical scheme is a highly suitable method for investigating cloud characteristics and feedback in GCMs and other large scale simulations of sub-stellar atmospheres. Split moment schemes and mixed material grains will be explored in a follow up study.

Key words. Planets and satellites: atmospheres – brown dwarfs – Methods: numerical

1. Introduction

JWST has revolutionised both the quantity and detail of data available for characterising the atmospheres of exoplanets and brown dwarfs. In addition to offering clearer signatures of the gas phase compositions of sub-stellar atmospheres compared to previous data, JWST provides valuable constraints on the global cloud components in these atmospheres through measuring their wavelength dependent impacts on the spectrum. This presents an opportunity to model and gain deeper insights into the 3D processes of cloud formation in these atmospheres. It also allows us to understand their feedback effects on thermal profiles, gas phase chemistry, and dynamical flows. Unveiling how each microphysical process affects global cloud structures and goes on to impact observed properties of sub-stellar objects will be key questions to answer in the coming years.

Before JWST's launch, several studies looked at the possibility of detecting the infrared features of cloud particle absorption by different condensates for hot Jupiter exoplanets (Wakeford & Sing 2015), as well as possibly inferring differences in the east-west limb-to-limb variance in cloud coverage (Parmentier et al. 2016; Powell et al. 2019). Recently, evidence for these effects in JWST data have been discovered, with silicate features

present in WASP-17b (Grant et al. 2023), WASP-107b (Dyrek et al. 2024), and HD 189733b (Inglis et al. 2024) as well as cloud and chemistry limb asymmetry found in WASP-39b (Espinoza et al. 2024) and WASP-107b (Murphy et al. 2024).

The evidence of limb asymmetry shows that cloud formation is inherently a 3D problem in gas giant atmospheres, with the microphysical properties of the clouds interacting with the dynamical flows of the atmosphere giving rise to this inhomogeneity. Moran et al. (2024) suggest that the shape of the SiO_2 absorption features in hot Jupiters could infer the specific temperature-pressure dependent crystal structure of the cloud particles, further linking the local atmospheric thermochemical environment to the observed cloud properties. Emission spectra are also aiding the characterisation of clouds, for example Bell et al. (2024) reported that the phase curve of WASP-43b showed consistent evidence of strong cloud coverage on the nightside of the planet. Schlawin et al. (2024) also reported strong temperature and cloud inhomogeneity on the dayside of WASP-69b from its JWST emission spectrum.

Studies coupling time-dependent clouds in multi-dimensional simulations for hot Jupiter atmospheres have been explored in recent years, with several schemes available in the literature. Lines et al. (2019) and Christie et al. (2021)

couple the diagnostic eddysed model of [Ackerman & Marley \(2001\)](#) to the Unified Model UK Met Office GCM to model the clouds on HD 209458b. [Komacek et al. \(2022\)](#) present a single moment saturation adjustment scheme with relaxation timescale based on the model presented in [Tan & Showman \(2019\)](#). This model was applied in an ultra hot Jupiter context in [Komacek et al. \(2022\)](#), with similar saturation adjustment schemes now being used by several groups (e.g. [Teinturier et al. 2024](#); [Lee et al. 2024](#)). [Lee et al. \(2016\)](#) and [Lines et al. \(2018\)](#) use a moment scheme based on the [Helling et al. \(2008\)](#) methodology coupled to a GCM to examine 3D cloud microphysics in the canonical hot Jupiters HD 189733b and HD 209458b. [Lee \(2023\)](#) present the ‘mini-cloud’ 4-moment scheme based on the asymptotic giant branch outflow dust formation theory in [Gail & Sedlmayr \(2013\)](#), with additions for ‘dirty’ mixed composition grains following [Helling et al. \(2008\)](#). [Powell & Zhang \(2024\)](#) used a pseudo-2D version of the CARMA bin microphysical cloud model ([Gao et al. 2018](#); [Gao & Benneke 2018](#)), showing a complex dynamic exchange of vapour and condensed species across the globe compared to static 1D models. They show that differences in cloud composition and particle sizes are driven by dynamical processes as well as microphysical processes. Despite this progress, modelling cloud microphysics self-consistently in exoplanet dynamical models remains a challenging prospect, but is key goal required for deeper understanding of the effect of clouds in hot Jupiter atmospheres.

In brown dwarf atmospheres, evidence of silicate features were seen in Spitzer IRAC data of L-dwarfs (e.g. [Cushing et al. 2006](#); [Suárez & Metchev 2022](#)), suggesting that active cloud formation was occurring in these objects. In addition, photometric surveys using ground based instruments and Spitzer showed signs of variability in T and L dwarf atmospheres, in particular at the L-T transition (e.g. [Radigan et al. 2014](#); [Apai et al. 2017](#); [Vos et al. 2019](#)), which suggested cloud formation was driving atmospheric variability. HST observations, sometimes with combined with Spitzer, also provided evidence of cloud driven spectral variability in some objects (e.g. [Yang et al. 2015](#); [Biller et al. 2018](#); [Bowler et al. 2020](#); [Zhou et al. 2020](#)), with large $\geq 10\%$ variations in the amplitude of the near-infrared H₂O features found in a variety of objects.

With this evidence of the effects of cloud coverage in brown dwarfs, the launch of JWST offers the ability to fully characterise the complexity of these clouds to understand their compositions, effect on the thermal and mixing properties of the atmosphere, and how they interact with chemical species. [Miles et al. \(2023\)](#) report a wide wavelength range spectrum of VHS 1256 b, finding disequilibrium chemistry and a silicate feature. [Biller et al. \(2024\)](#) recently published spectral variability light curves across the NIRSpec Prism and MIRI Low Resolution Spectrograph (LRS) wavelength ranges for WISE 1049A and WISE 1049B, finding evidence for chemical species and cloud coverage variability in their atmospheres, in addition to a variable silicate absorption feature for WISE 1049A. This suggests a strongly inhomogenous atmosphere with dynamically driven small and large scale dynamical features forming and dissipating in these atmospheres at shorter timescales than the rotational period.

Previous theoretical and modelling studies of brown dwarfs have revealed the time-dependent connection between atmospheric temperatures, dynamics, cloud coverage and chemistry. [Zhang & Showman \(2014\)](#) used a pulsing thermal perturbation scheme to imitate the temperature forcing induced by convection near the radiative-convective boundary coupled to a global shallow-water model. They found the strength of the atmo-

spheric temperature variability greatly depended on the dynamical regime of the atmosphere. [Robinson & Marley \(2014\)](#) used a 1D model with deep temperature perturbations to investigate the connection between deep convective motions and the observed spectral features. [Morley et al. \(2014\)](#) modeled variability of T- and Y-dwarfs with patchy sulfide and salt cloud layers. [Tan & Showman \(2019\)](#) find that cloud opacity feedback can trigger convective motions, giving rise to cloud condensation and evaporation cycles. [Tremblin et al. \(2020\)](#) apply modified temperature-pressure (T-p) profiles to mimic thermal variability and also investigate the effects of non-equilibrium chemistry on the variability and strength of spectral features. [Luna & Morley \(2021\)](#) use the [Ackerman & Marley \(2001\)](#) equilibrium cloud model to produce vertical cloud profiles that attempt to fit the Spitzer IRS silicate feature in brown dwarfs ([Cushing et al. 2006](#); [Looper et al. 2008](#)) and Spitzer photometric band variability ([Metchev et al. 2015](#)). [Hammond et al. \(2023\)](#) found four main dynamical regimes for brown dwarfs, depending on the non-dimensional radiative timescale and thermal Rossby number. [Lacy & Burrows \(2023\)](#) show significant effects when considering the impact of H₂O clouds on Y-dwarf thermal structures. [Lee et al. \(2023\)](#) and [Lee et al. \(2024\)](#) examine the impact of large scale dynamical features in brown dwarfs and directly imaged exoplanets on the 3D chemical, cloud and variability characteristics of the atmosphere.

Owing to the continued release of JWST data starting to characterise the cloud structures of sub-stellar atmospheres in detail, microphysical models are warranted to deeply understand the processes that give rise to the specific features and effects seen in the spectra of sub-stellar objects. Bulk, also known as moment, schemes remain a popular option in Earth Science for modelling cloud microphysics due to their relative simplicity and computational efficiency (for review, see e.g., [Morrison et al. 2020](#)). Only a few moments (in this paper, two) are required to be evolved in the dynamical system, with each moment representing an average value of the particle size distribution and the microphysical processes altering these mean values in time.

For sub-stellar atmospheres, bulk schemes have been developed by a few groups (e.g. [Helling et al. 2008](#); [Ohno & Okuzumi 2017, 2018](#); [Ormel & Min 2019](#); [Woitke et al. 2020](#); [Lee 2023](#); [Huang et al. 2024](#)) but only a few studies have used bulk schemes directly coupled time-dependently to 3D atmospheric simulations (e.g. [Lee et al. 2016](#); [Lines et al. 2018](#); [Lee 2023](#)). Bulk schemes are contrasted with bin or spectral models (e.g. CARMA, [Gao et al. 2018](#)), which evolve the discretised particle size distribution in time through calculating the fluxes in and out each bin size. Typically 40-70 or more mass or size bins are required to adequately resolve the size distribution in these models (e.g. [Adams et al. 2019](#)), making them much more computationally demanding than bulk methods and more challenging to include in large scale 3D atmospheric modelling with present resources.

In this study, we expand the mini-cloud code package ([Lee 2023](#)) to include a new 2-moment cloud microphysical scheme able to be efficiently coupled to time-dependent sub-stellar atmosphere simulations in a simple manner. The present 2-moment scheme also newly implements the collision growth of cloud particles, which is a key process to produce rain droplets in Earth clouds ([Morrison et al. 2020](#)). In Section 2, we present the mass moment scheme and detail the individual microphysical source and sink terms in the set of ordinary differential equations (ODEs). In Section 3, we couple our new 2-moment scheme to the 3D Exo-FMS GCM to simulate a Y-dwarf as a test application. In Section 5, we post-process our simulation and gener-

ate emission spectra and variability light curves. In Section 6, we discuss our results in context to other modelling efforts and observational data. Section 7 contains the summary and conclusions of our study. Each of the new moment schemes are available online¹.

2. Bulk microphysical scheme

For this study, we consider the mass moments of the particle mass distribution. The mass moments, $M^{(k)}$ [$\text{g}^k \text{cm}^{-3}$], of the particle mass distribution are given by

$$M^{(k)} = \int_0^\infty m^k f(m) dm, \quad (1)$$

where k is the integer moment power, m [g] the mass of a particle in the distribution and $f(m)$ [$\text{cm}^{-3} \text{g}^{-1}$] the particle mass distribution.

Examining the moments up to the second ($k = 2$), leads to a set of moments each with physical meanings that represent bulk values of the particle size distribution:

$$M^{(0)} = N_c, \quad (2)$$

in units of cm^{-3} which represents the total number density of the size distribution,

$$M^{(1)} = \rho_c, \quad (3)$$

in units of g cm^{-3} which represents the total mass density of the size distribution, and

$$M^{(2)} = Z_c, \quad (4)$$

in units of $\text{g}^2 \text{cm}^{-3}$ which is related to the Rayleigh regime radar reflectivity of the size distribution². Z_c is typically divided by the square of the atmospheric density ρ_a [g cm^{-3}], giving it the more regular units of $\text{cm}^6 \text{cm}^{-3}$. Here the subscript c stands for ‘cloud’ particles, but different sub-scripts can be used to distinguish various aerosol types such as haze (e.g. Ohno 2024). Note that the mass moments have equivalents when taking moments of the radius distribution (e.g. Gail & Sedlmayr 2013), N_c is the zeroth moment, ρ_c the third moment and Z_c the sixth moment in radius space respectively.

Ratios and relationships between each of the moments provides information on the characteristics of the particle size distribution, for example the mean mass of a particle, m_c [g], is given by the ratio of the first to zeroth moment

$$m_c = \frac{\rho_c}{N_c}, \quad (5)$$

and the average particle volume, V_c [cm^3],

$$V_c = \frac{m_c}{\rho_d}, \quad (6)$$

where ρ_d [g cm^{-3}] is the bulk mass density of the particle, which is not necessary the material mass density if the particle porosity

¹ https://github.com/ELeeAstro/mini_cloud

² In other words, Z_c is related to scattering efficiency of clouds. The scattering cross section of a cloud particle obeys $\sigma_{\text{Ray}} \propto a^6 \propto m^2$ in the Rayleigh regime (e.g., Bohren & Huffman 1983). This yields a scattering efficiency $= \int \sigma_{\text{Ray}} f(m) dm$ being proportional to Z_c .

is taken into account (e.g., Ohno et al. 2020). The mass or volume weighted mean particle radius, r_c [cm], can be derived as

$$r_c = \sqrt[3]{\frac{3m_c}{4\pi\rho_d}}. \quad (7)$$

The standard deviation, σ_c [g], of the mass distribution can be characterised through (e.g. Gail & Sedlmayr 2013)

$$\sigma_c = \sqrt{\frac{Z_c}{N_c} - \left(\frac{\rho_c}{N_c}\right)^2}. \quad (8)$$

Following the general method for deriving the time derivatives of the moments (e.g. Gail & Sedlmayr 2013), Appendix A, the set of differential equations for the 2-moment scheme used in this study are given by

$$\frac{dN_c}{dt} = (J_{\text{hom}} + J_{\text{evap}}) + \left(\frac{dN_c}{dt}\right)_{\text{coll}}, \quad (9)$$

$$\frac{d\rho_c}{dt} = m_{\text{seed}}(J_{\text{hom}} + J_{\text{evap}}) + \left(\frac{dm}{dt}\right)_{\text{cond}} N_c, \quad (10)$$

where J_{hom} [$\text{cm}^{-3} \text{s}^{-1}$] is the homogeneous nucleation rate of seed particles, J_{evap} [$\text{cm}^{-3} \text{s}^{-1}$] is the prescribed disappearance rate of seed particles through evaporation, and m_{seed} is the mass of a seed particle. The change in condensable vapour mass density, ρ_v [g cm^{-3}], is given by

$$\frac{d\rho_v}{dt} = -m_{\text{seed}}(J_{\text{hom}} + J_{\text{evap}}) - \left(\frac{dm}{dt}\right)_{\text{cond}} N_c + \left(\frac{d\rho_v}{dt}\right)_{\text{deep}}. \quad (11)$$

In the current 2-moment scheme, we have assumed a monodisperse size distribution that can be uniquely identified by N_c and ρ_c (Appendix A). Thus, we ignore the second moment, Z_c , and only evolve N_c , ρ_c and ρ_v with time. We detail each of the source and sink terms in the following sections.

2.1. Collisional growth processes

Collisional growth rates are primarily governed by the Smoluchowski equation (Smoluchowski 1916) in its continuous form (Müller 1928)

$$\begin{aligned} \frac{\partial n(m)}{\partial t} = & -n(m) \int_0^\infty K(m, m') n(m') dm' \\ & + \frac{1}{2} \int_0^m K(m - m', m') n(m - m') n(m') dm', \end{aligned} \quad (12)$$

where m [g] and m' [g] are discrete particle masses of the distribution, $n(m)$ [cm^{-3}] the number density of particles of mass m and K [$\text{cm}^3 \text{s}^{-1}$] the collisional probability rate between two particle masses, typically called the collision kernel.

In Drake (1972), the mass moment generative function of the Smoluchowski equation is derived as

$$\begin{aligned} \frac{dM^{(k)}}{dt} = & \frac{1}{2} \int_0^\infty \int_0^\infty K(m, m') f(m) f(m') \\ & \times [(m + m')^k - m^k - m'^k] dm dm', \end{aligned} \quad (13)$$

where m and m' represent different masses in the particle mass distribution. We can immediately get expressions for the zeroth and first moments, N_c and ρ_c , for $k = 0$ and 1 respectively

$$\frac{dN_c}{dt} = -\frac{1}{2} \int_0^\infty \int_0^\infty K(m, m') f(m) f(m') dm dm', \quad (14)$$

$$\frac{d\rho_c}{dt} = 0. \quad (15)$$

These rate expressions follow the expected behaviour for collisional growth interactions. For the zeroth moment, collisional growth is a sink term, reducing the number density with time and total mass is conserved during collisions, recovering a zero rate for the first moment.

The total rate of change of the zeroth moment given by collisional growth is the combination of the coagulation and coalescence processes

$$\left(\frac{dN_c}{dt}\right)_{\text{coll}} = \left(\frac{dN_c}{dt}\right)_{\text{coag}} + \left(\frac{dN_c}{dt}\right)_{\text{coal}}. \quad (16)$$

Throughout we assume ‘hit-and-stick’ collisions, ignoring other effects such as bouncing and fragmentation. We do not include turbulence driven collisional processes in this study, such as those considered in [Samra et al. \(2022\)](#), since the energy dissipation rate of turbulence remains highly uncertain for brown dwarfs and exoplanets.

2.1.1. Brownian coagulation

In collisional growth via Brownian motion (coagulation), particles interact via random walk, the rate of which depend on the local atmospheric properties and particle characteristics. This is primarily dependent on the Knudsen number, Kn, regime

$$\text{Kn} = \frac{\lambda_a}{r_c}, \quad (17)$$

where λ_a [cm] is the mean free path of the atmosphere given by

$$\lambda_a = \frac{2\eta_a}{\rho_a} \sqrt{\frac{\pi\bar{\mu}_a}{8RT}}, \quad (18)$$

where $\bar{\mu}_a$ [g mol⁻¹] is the local atmospheric mean molecular weight, ρ_a [g cm⁻³] the mass density of the atmosphere and the dynamical viscosity, η_a [g cm⁻¹ s⁻¹], of the atmosphere given by the [Rosner \(2012\)](#) fitting function

$$\eta_a = \frac{5}{16} \frac{\sqrt{\pi m k_b T} (k_b T / \epsilon_{LJ})^{0.16}}{\pi d^2 1.22}, \quad (19)$$

where the parameters for the molecular diameter, d [cm], mass, m [g], and Lennard-Jones potential, ϵ_{LJ} , for H₂, He and H, the main components of hydrogen-rich atmospheres are listed in [Lee \(2023\)](#), though in mini-cloud we include values taken from [Rosner \(2012\)](#) to account for the gas species used in the mini-chem chemical kinetics scheme ([Tsai et al. 2022](#)).

The dynamical viscosity of mixtures of gas species can be calculated from weighting the dynamical viscosity of each species with their local volume mixing ratios following the approximate classical mixing law from [Wilke \(1950\)](#) or the approximate square root mixing law from [Herning & Zipperer \(1936\)](#). A more complex mixing law, taking into account the momentum

exchange between gas species can also be used ([Davidson 1993](#); [Gao et al. 2023](#)). Here, we use the [Wilke \(1950\)](#) mixing rule.

To derive the set of coagulation rate equations, we follow the arguments in [Rossow \(1978\)](#) for similar sized particle-particle collisions at the mean particle size, r_c . [Rossow \(1978\)](#) considers the coagulation collision kernel expression from [Fuchs \(1964\)](#) but here we consider the kernel following [Chandrasekhar \(1943\)](#) valid in the Kn $\ll 1$ regime

$$K = 4\pi [D(r) + D(r')] (r + r'), \quad (20)$$

where $D(r)$ is the particle diffusion factor given by ([Chandrasekhar 1943](#))

$$D(r) = \frac{k_b T \beta}{6\pi\eta_a r}, \quad (21)$$

where β is the Cunningham slip correction factor ([Davies 1945](#))

$$\beta = 1 + \text{Kn} [1.275 + 0.4 \exp(-1.1/\text{Kn})]. \quad (22)$$

Assuming similar sized collisions ($r \approx r'$, $m \approx m'$) at the mean particle size r_c , applying this kernel expression into Eq. 14 gives

$$\left(\frac{dN_c}{dt}\right)_{\text{coag}} \approx -\frac{4k_b T \beta}{3\eta_a} N_c^2. \quad (23)$$

For the free molecular flow or kinetic regime (Kn $\gg 1$), a Maxwell-Boltzmann thermal velocity distribution can be assumed for the particles. [Rossow \(1978\)](#) uses the [Brock & Hidy \(1965\)](#) collision kernel but to facilitate clearer calculations we follow the [Vincenti & Kruger \(1965\)](#) kernel given by

$$K = (r + r')^2 \sqrt{\frac{8\pi k_b T}{\bar{m}}}, \quad (24)$$

where $\bar{m} = mm'/(m + m')$ [g] is the reduced mass. Again, assuming similar sized collisions ($r \approx r'$, $m \approx m'$) at the mean particle size r_c and putting this kernel into Eq. 14 yields

$$\left(\frac{dN_c}{dt}\right)_{\text{coag}} \approx -8 \sqrt{\frac{\pi k_b T}{m_c}} r_c^2 N_c^2. \quad (25)$$

Overall, Eqs. 23 and 25 are same expressions found in [Ohno & Okuzumi \(2018\)](#) and [Ohno et al. \(2020\)](#), which we here derived directly from the [Drake \(1972\)](#) formulation.

An approach including an interpolation function between the continuum and kinetic regimes is also commonly used in the literature (e.g. [Fuchs 1964](#); [Pruppacher & Klett 1978](#); [Lavvas et al. 2010](#); [Gao et al. 2018](#)). In this case, the coagulation kernel is given by ([Gao et al. 2018](#))

$$K = \frac{4\pi [D(r) + D(r')] (r + r')}{\frac{r+r'}{r+r'+\sqrt{\delta_r^2+\delta_r'^2}} + \frac{4[D(r)+D(r')]}{(r+r')\sqrt{V_r^2+V_r'^2}}}, \quad (26)$$

where V_r is

$$V_r = \sqrt{\frac{8k_b T}{\pi m_r}}, \quad (27)$$

and δ_r is

$$\delta_r = \frac{(2r + \lambda_r)^3 - (4r^2 + \lambda_r^2)^{3/2}}{6r\lambda_r} - 2r, \quad (28)$$

where λ_r

$$\lambda_r = \frac{8D(r)}{\pi V_r}. \quad (29)$$

δ_r is the function that interpolates between the continuum (Eq. 23) and kinetic (Eq. 25) regimes.

Again, assuming similar sized collisions, $r \approx r'$ at the mean particle size r_c , this kernel reduces to

$$K = \frac{16\pi D(r_c)r_c}{\frac{2r_c}{2r_c + \sqrt{2}\delta_{r_c}} + \frac{4D(r_c)}{r_c\sqrt{2}V_{r_c}}}. \quad (30)$$

Defining the correction factor as

$$\varphi = \frac{2r_c}{2r_c + \sqrt{2}\delta_{r_c}} + \frac{4D(r_c)}{r_c\sqrt{2}V_{r_c}}, \quad (31)$$

and putting this kernel into Eq. 14 gives

$$\left(\frac{dN_c}{dt}\right)_{\text{coag}} \approx -\frac{4k_b T \beta}{3\eta_a \varphi} N_c^2. \quad (32)$$

Due to the versatility of the interpolation function approach, we primarily make use of Eq. 32 in mini-cloud.

2.1.2. Gravitational coalescence

When there is a difference in the settling velocity between two different particle sizes, the larger particle settles faster, impacting and coalescing with the slower moving particles below. The kernel for gravitational coalescence is given by (e.g. Jacobson 2005)

$$K = \pi(r + r')^2 |v_f(r) - v_f(r')| E, \quad (33)$$

where $r' > r$, $v_f(r)$ [cm s⁻¹] the settling velocity and E the collisional efficiency factor. Defining the differential settling velocity as $\Delta v_f = |v_f(r) - v_f(r')|$ and assuming similar particle size collisions ($r \approx r'$) at the mean particle size r_c , the differential equation for the zeroth moment is, following Eq. 14,

$$\left(\frac{dN_c}{dt}\right)_{\text{coal}} \approx -2\pi r_c^2 \Delta v_f E N_c^2. \quad (34)$$

Following Ohno & Okuzumi (2017) to evaluate Δv_f we introduce a parameter, ϵ , that estimates the relative velocity of the particles from the mean particle size settling velocity, $v_f(r_c)$, giving $\Delta v_f \approx \epsilon v_f(r_c)$. This is taken as $\epsilon \approx 0.5$ following the results of Sato et al. (2016), who found this value to best reproduce the results of a collisional bin resolving model for grain growth in protoplanetary disks. The settling velocity is given by the expression in Ohno & Okuzumi (2018)

$$v_f(r_c) = \frac{2\beta g r_c^2 \rho_d}{9\eta_a} \left[1 + \left(\frac{0.45 g r_c^3 \rho_a \rho_d}{54\eta_a^2} \right)^{2/5} \right]^{-5/4}, \quad (35)$$

where g [cm s⁻²] is the gravity. E is a collisional efficiency factor, dependent on the Stokes number, Stk ,

$$\text{Stk} = \frac{\Delta v_f v_f(r_c)}{g r_c} = \frac{\epsilon v_f^2(r_c)}{g r_c}. \quad (36)$$

E is then given by (Guillot et al. 2014)

$$E = \begin{cases} \max\left[0, 1 - 0.42\text{Stk}^{-0.75}\right] & \text{Kn} < 1 \\ 1 & \text{Kn} \geq 1 \end{cases} \quad (37)$$

2.2. Condensation and evaporation

Condensation occurs when a condensable vapour species is supersaturated with respect to its saturation vapour pressure, while evaporation occurs when the vapour is under-saturated. In the small Knudsen number regime $\text{Kn} \ll 1$, the growth of the particle is limited by the diffusion of condensable gas to the surface of the grain. In this regime, we follow the derivation found in Woitke & Helling (2003) but defined for mass instead of volume

$$\left(\frac{dm}{dt}\right)_{\text{cond}} = 4\pi r_c D m_0 n_v \left(1 - \frac{1}{S}\right), \quad (38)$$

where $S(T) = p_{\text{par}}/p_{\text{vap}}(T)$ is the supersaturation ratio, the ratio of the condensate vapour partial pressure, p_{par} [dyne cm⁻²], to the saturation vapour pressure, $p_{\text{vap}}(T)$ [dyne cm⁻²], m_0 [g] the mass of one molecular unit of the condensate and n_v [cm⁻³] the number density of the condensing vapour. The gaseous diffusion constant, D [cm² s⁻¹], can be given by (Jacobson 2005)

$$D = \frac{5}{16N_A d_i^2 \rho_a} \sqrt{\frac{RT \bar{\mu}_a}{2\pi} \left(\frac{\mu_v + \bar{\mu}_a}{\mu_v}\right)}, \quad (39)$$

where N_A is Avogadro's number, d_i [cm] the collision diameter, and μ_v the molecular weight of the condensable vapour.

In the free molecular regime, $\text{Kn} \gg 1$, the condensation rate is given by (Woitke & Helling 2003)

$$\left(\frac{dm}{dt}\right)_{\text{cond}} = 4\pi r_c^2 v_{\text{th}} m_0 n_v \left(1 - \frac{1}{S}\right), \quad (40)$$

where $v_{\text{th}} = \sqrt{k_b T / 2\pi m_v}$ [cm s⁻¹] is the thermal velocity of the condensable vapour, with m_v [g] the mass of the condensable vapour. We note that we have ignored the effects of latent heat and the Kelvin effect in Eqs. 38 and 40, which can be modified to take into account these and additional kinetic effects near the surface of the grain (e.g. Toon et al. 1989b; Lavvas et al. 2011; Gao et al. 2018).

2.3. Homogeneous nucleation

Homogeneous nucleation is the processes by which supersaturated vapour of a single gas species forms clusters of molecules which, in favourable thermochemical conditions, can then overcome the energy barrier of the nucleation process. These clusters can then grow to form seed particle sized solid materials of ~ 1 nm, and provide surfaces for condensable species to interact with. This makes homogeneous nucleation an important consideration, as this process is responsible for forming the first surfaces, or cloud condensation nuclei (CCN), in the cloud formation system.

We follow the modified classical nucleation theory (MCNT) first outlined in Draine & Salpeter (1977) and Gail et al. (1984), examined in a sub-stellar atmosphere context in several studies (e.g. Helling & Fomins 2013; Lee et al. 2018; Sindel et al. 2022; Kiefer et al. 2023). The homogeneous nucleation rate, J_{hom} [cm⁻³ s⁻¹], is given by (Helling & Fomins 2013)

$$J_{\text{hom}} = \frac{\dot{f}(1)}{\tau_{\text{gr}}(1, N_*)} Z(N_*) \exp\left[(N_* - 1) \ln S(T) - \frac{\Delta G(N_*)}{RT}\right], \quad (41)$$

where $\dot{f}(1)$ [cm⁻³] is the equilibrium number density of the nucleating vapour and $\tau_{\text{gr}}(1, N_*)$ [s] the growth timescale of the

critical cluster size N_* given by

$$\tau_{\text{gr}}^{-1} = 4\pi r_0^2 N_*^{2/3} \alpha n_v \sqrt{\frac{k_b T}{2\pi m_0}}, \quad (42)$$

where r_0 [cm] is the vapour monomer radius, α an efficiency factor and n_v [cm⁻³] the number density of the nucleating vapour. The Gibbs free energy expression is given by

$$\frac{\Delta G(N)}{RT} = \theta_\infty \frac{N-1}{(N-1)^{1/3} + N_f^{1/3}} \quad \text{with} \quad \theta_\infty = \frac{4\pi r_0^2 \sigma_\infty}{k_b T}, \quad (43)$$

where $\sigma_\infty(T)$ [erg cm⁻²] is the bulk surface tension and N_f a fitting factor parameter. The critical cluster size, N_* , is

$$N_* - 1 = \frac{N_{*,\infty}}{8} \left[1 + \sqrt{1 + 2 \left(\frac{N_f}{N_{*,\infty}} \right)^{1/3}} - 2 \left(\frac{N_f}{N_{*,\infty}} \right)^{1/3} \right]^3, \quad (44)$$

with

$$N_{*,\infty} = \left(\frac{\frac{2}{3}\theta_\infty}{\ln S(T)} \right)^3. \quad (45)$$

The Zeldovich factor, Z , is

$$Z(N_*) = \left[\frac{\theta_\infty}{9\pi(N_* - 1)^{4/3}} \frac{\left(1 + 2 \left(\frac{N_f}{N_* - 1} \right)^{1/3} \right)}{\left(1 + \left(\frac{N_f}{N_* - 1} \right)^{1/3} \right)^3} \right]^{1/2}. \quad (46)$$

For KCl homogeneous nucleation, we assume $\alpha = 1$, $N_f = 10$ and the temperature dependent surface tension expression from Janz (2013).

2.4. Seed particle evaporation

Should all condensed species be evaporated from the surface of the particles, the seed particle core may evaporate back into the vapour phase. If the average mass of the particles is within 0.1% of the seed particle mass ($m_c < 1.001 m_{\text{seed}}$) and $dm/dt < 0$ we assume that the core is exposed to the atmosphere and undergoes evaporation. The evaporation rate of seed particles, J_{evap} [cm⁻³ s⁻¹], is approximated as

$$J_{\text{evap}} = -\frac{N_c}{\tau_{\text{evap}}}, \quad (47)$$

where τ_{evap} is the seed particle evaporation timescale. The evaporation rate of seed particles can be estimated as $\tau_{\text{evap}} = m_{\text{seed}}/|dm/dt|$ (Lee 2023). However, this can prove numerically unstable, especially in strong evaporating regions. We therefore prefer a parameterised approach, adopting $\tau_{\text{evap}} = 1$ s in mini-cloud, which results in a smoother seed particle evaporation profile but still removing seed particles from regions of strong evaporation in one or two typical timesteps.

2.5. Condensate vapour replenishment

The atmosphere is continually refreshed with condensable vapour and excess vapour mixed deeper through connection with the interior, typically assumed to occur through deep convective motions. To mimic this, at the bottom most layer only, we follow the relaxation approach from Komacek et al. (2022) given by

$$\left(\frac{d\rho_v}{dt} \right)_{\text{deep}} = -\frac{\rho_v - \rho_{\text{deep}}}{\tau_{\text{deep}}}, \quad (48)$$

where ρ_{deep} [g cm⁻³] is the deep condensate vapour density and τ_{deep} [s] the deep replenishment timescale. The deep replenishment timescale can be set as a parameter or estimated from

$$\tau_{\text{deep}} = \frac{\alpha_{\text{mix}} H_{\text{p,deep}}^2}{K_{\text{zz,deep}}}, \quad (49)$$

where $H_{\text{p,deep}}$ [cm] is the atmospheric scale height, $K_{\text{zz,deep}}$ [cm² s⁻¹] the eddy diffusion coefficient at the lowest layer respectively. α_{mix} is a scaling parameter that estimates the number of atmospheric scale heights of the mixing region in the deep atmosphere.

3. Application to Y-dwarf KCl clouds

In an initial test of our cloud scheme, we use the Exo-FMS GCM (e.g. Lee et al. 2021) following the simulation setup of Lee et al. (2024), but replacing the Komacek et al. (2022) saturation adjustment cloud model with our microphysical 2-moment scheme. All other physics and chemistry modules are kept as in Lee et al. (2024), which includes mixing length theory (MLT), correlated-k radiative-transfer and the mini-chem kinetic chemistry scheme. We assume a minimum $K_{\text{zz}} = 10^5$ cm² s⁻¹ diffusive mixing in the atmosphere, which is an estimate of the natural background minimal vertical mixing occurring in the radiative region of sub-stellar atmospheres (e.g. Christie et al. 2021). We model a Y-dwarf with $T_{\text{int}} = 400$ K, [M/H] = 0, log g = 4.25 in order to directly compare to the 1D Gao et al. (2018) study who applied the CARMA microphysical bin model to the same parameters. Following Showman et al. (2019), the thermal perturbation amplitude at the radiative-convective boundary (RCB) is estimated to be $\sim 10^{-6}$ K s⁻¹. We assume a RCB at 40 bar from the results of convection resolving models (Lee et al. in prep.). We assume a Jupiter-like rotation rate of 10 hours.

The weak forcing regime and weak vertical mixing allows a quick statistical convergence of the atmospheric dynamics and composition, on par with the convergence rates for hotter objects simulated in Tan & Showman (2021). We perform the first 100 days of simulation with the cloud component but without thermal feedback, after which the cloud opacity is ramped up slowly for the next 100 days. The simulation including the full cloud opacity is then performed for the final 300 days. To examine the variability characteristics, we then run the model for an additional 72 hours, taking snapshots every hour of the simulation output.

The chemical equilibrium deep volume mixing ratio of KCl is $\approx 10^{-7}$ at [M/H] = 0 (Woitke et al. 2018), which we assume is the deep reservoir condensable vapour abundance. We assume all Na has condensed in the atmosphere and do not include the opacity of gas phase Na and K in the GCM. We assume an initial cloud and condensable vapour free atmosphere, with the lower boundary of the atmosphere assumed to be cloud free and replenished to the deep vapour reservoir value across each timestep. We use the DLSODE³ stiff ordinary differential equation solver (Radhakrishnan & Hindmarsh 1993) to integrate the coupled ODE system inside the GCM.

We assume a pure KCl cloud composition with $\rho_d = 1.99$ g cm⁻³, $\mu_v = 74.55$ g mol⁻¹, $r_{\text{seed}} = 1$ nm. The vapour pressure expression for KCl is taken from Morley et al. (2012) and temperature dependent surface tension expression from Janz (2013). Background gas conditions are self-consistently calculated in the GCM from the local T-p conditions and volume mixing ratios of

³ <https://computing.llnl.gov/projects/odepack/software>

Table 1. Adopted Exo-FMS GCM simulation parameters for the test Y-dwarf simulation. We use a cubed-sphere resolution of C48 ($\approx 192 \times 96$ in longitude \times latitude).

Symbol	Value	Unit	Description
T_{int}	400	K	Internal temperature
p_0	100	bar	Reference surface pressure
p_{up}	10^{-4}	bar	Upper boundary pressure
c_p	12039	$\text{J K}^{-1} \text{kg}^{-1}$	Specific heat capacity
R_d	3568	$\text{J K}^{-1} \text{kg}^{-1}$	Specific gas constant
κ	0.296	-	Adiabatic coefficient
g_p	178	m s^{-2}	Gravitational acceleration
R_p	$7.149 \cdot 10^7$	m	Planetary radius
Ω_p	$1.746 \cdot 10^{-4}$	rad s^{-1}	Rotation rate
[M/H]	0	-	\log_{10} solar metallicity
p_{amp}	40	bar	Perturbation boundary layer
T_{amp}	10^{-6}	K s^{-1}	Perturbation amplitude
α	1	-	MLT scale parameter
β	2.2	-	Overshooting parameter
τ_{storm}	10^5	s	Storm timescale
τ_{drag}	10^7	s	Basal drag timescale
Δt_{hyd}	60	s	Hydrodynamic time-step
Δt_{rad}	600	s	Radiative time-step
Δt_{MLT}	0.5	s	Mixing length theory time-step
Δt_{ch}	600	s	mini-chem time-step
Δt_{cld}	600	s	mini-cloud time-step
N_v	60	-	Vertical resolution
d_4	0.16	-	$O(4)$ divergence dampening coef.

gas phase species from the mini-chem kinetic chemistry module. In the GCM, the moment values are converted to volume or mass mixing ratios through the relations

$$q_0 = \frac{N_c}{n_a}, \quad (50)$$

$$q_1 = \frac{\rho_c}{\rho_a}, \quad (51)$$

and

$$q_v = \frac{\rho_v}{\rho_a}, \quad (52)$$

where n_a [cm^{-3}] is the atmospheric number density. These mixing ratio tracers are the advected quantities inside the GCM dynamical core and other transport routines such as vertical settling and diffusion.

Eq. 35 is used to calculate the settling velocities for the cloud particles inside the GCM. We assume the settling velocity for all moments to occur at the mass weighted mean particle radius, r_c , as given by Eq. 7. This approximation is valid when the size distribution can be approximated by the delta function, as adopted in the current 2-moment model. Strictly, each moment should have its own settling velocity (e.g. [Woitke et al. 2020](#)) as intuitively different parts of the particle size distribution, represented by the moment values, should settle at different rates (see also [Appendix A](#)). However, this can lead to difficult to resolve numerical issues if a moment can settle faster into a layer where the other moments are negligible.

3.1. Cloud opacity feedback

To calculate the wavelength dependent cloud opacity, single scattering albedo and asymmetry factor, we follow a similar

scheme to the cloud opacity calculations in [Lee \(2023\)](#). For small size parameters ($x < 0.01$) the Rayleigh limit expressions are used ([Bohren & Huffman 1983](#)) and for large size parameters ($x > 10$) Modified Anomalous Diffraction Theory (MADT) is used following [Moosmüller & Sorensen \(2018\)](#). For intermediate size parameters, the LX-MIE code of [Kitzmann & Heng \(2018\)](#) is applied. We assume a well peaked, monodisperse distribution, where r_c is a representative size for the opacity of the size distribution. This can lead to inaccuracy when considering the full particle size distribution (e.g. [Appendix B](#)), but is much faster to calculate and amenable to large scale simulations such as GCMs. We take the real and imaginary refractive indices of KCl salt from [Palik \(1985\)](#) and [Querry \(1987\)](#). The MADT approach typically results in inaccuracies when the real refractive index is large ($n \gtrsim 1.5$), which the real index of KCl reaches frequently across the wavelength regime of the database tables. However, compared to the full Mie calculation, MADT offers much more computational efficiency for the large size parameter regime while retaining the salient effects of cloud opacity feedback, making it highly useful for large scale simulations such as GCMs.

For the asymmetry parameter, we assume $g = 0$ for the Rayleigh regime, and take the value from LX-MIE for the intermediate size parameter regime. However, MADT cannot directly calculate the asymmetry parameter, and so we follow the parametrisation from [Ehlers & Moosmüller \(2023\)](#)

$$g = \min[C(m)x^2, 0.9], \quad (53)$$

where $C(m)$ is a function of the complex refractive index ([Ehlers & Moosmüller 2023](#)). We limit g to a maximum of 0.9 to attempt to capture the leveling off of the asymmetry parameter at large size parameters (e.g. [Cuzzi et al. 2014](#)) and avoid unphysical values of g .

4. Y-dwarf GCM results

Figure 1 shows the zonal mean zonal velocity and zonal mean vertical velocity. This generally shows a very stagnant atmosphere, with most of the atmosphere having near zero zonal and vertical velocity outside of the equatorial regions. Weak jet features are seen at the equator, on the order of $\sim 100 \text{ m s}^{-1}$, on the order of Jupiter's equatorial jet speed (e.g. Porco et al. 2003). Very weak vertical velocities are produced, on the order of $\sim 10^{-4} \text{ m s}^{-1}$, resulting in a very sluggish and stagnant atmosphere. We find that MLT is not triggered later in the simulation, suggesting strong static stability in the atmosphere.

In Figure 2, we present latitude-longitude maps of the atmosphere at 0.3 bar for different variables. This shows that the main dynamical features occur at the equatorial region of the atmosphere, with higher latitudes well homogenised in temperature, cloud properties and chemical composition. However, the atmosphere is generally extremely homogenised, with only $\sim 3 \text{ K}$ variations in temperatures across the globe at the 0.3 bar pressure level and only a $\sim 2 \text{ K}$ variation in bolometric brightness temperature. Only minor variations in particle size and particle number density are seen between the equatorial regions and the higher latitudes. The bolometric temperature maps are not equal to the prescribed internal temperature of $T_{\text{int}} = 400 \text{ K}$, suggesting the atmosphere is not in radiative-convective equilibrium and may still be evolving. Otherwise, additional energy may be put into the system through the convective perturbation scheme or inaccuracy of the Toon et al. (1989a) radiative-transfer scheme used in this study (e.g. Rooney et al. 2024) leading to inaccurate heating rates, especially when a strong scattering component such as clouds are present.

Due to the high homogeneity and stagnation, some small scale cube-sphere grid artefacts are present at mid-latitudes, most noticeable in the higher colour contrast bolometric brightness temperature and cloud particle number density plots in Figure 2. However, these variations are highly minor with only a $\lesssim 1 \text{ K}$ variation in brightness temperature and atmospheric temperature and do not induce any significant dynamical processes in the atmosphere.

These artefacts are likely numerical in origin, probably related to numerical errors at the cube-sphere boundaries when calculating gradients in a slow moving atmosphere. We attempted to reduce these artefacts through including stronger numerical hyper-diffusion and different initial conditions without success, suggesting that this dynamical regime may have numerical errors at special grid boundaries on the order of the absolute horizontal and vertical velocity (e.g. see Putman & Lin 2007). Figure 1 suggests the vertical and zonal velocities are near zero across most of the atmosphere, with vertical velocities near or below the natural numerical error boundary for the Exo-FMS cube-sphere grid (Putman & Lin 2007). This is therefore the likely origin of the cube-sphere grid imprint. Points internal to the boundary do not show any grid artefacts, suggesting the reduction in the order of accuracy near the boundaries are the main cause of the imprint. It is unclear whether other GCMs with different grid layouts would produce these artefacts in similar conditions, or if they can be alleviated through other methods. Despite these artefacts, they produce very minor perturbations, and the main conclusions of cloud characteristics in this study are unaffected.

In Figure 3, we present globally averaged values of the GCM simulation. Our KCl cloud structure shows a typical cloud profile, with larger grains, in this case $\sim 1 \mu\text{m}$, settling to the cloud base, before evaporating. Only very small particles $\approx 3 \cdot 10^{-2} \mu\text{m}$ can remain lofted in the upper atmospheres. We find that MLT is

not triggered in the atmosphere, suggesting the T-p profile is in strong static stability, and mixing is dominated by the imposed $K_{zz} = 10^5 \text{ cm}^2 \text{ s}^{-1}$ minimum. The KCl clouds have a minimal impact on the T-p profile of the atmosphere, suggesting that the gas phase opacity is much larger than the cloud opacity in this case, similar to previous findings that examined KCl cloud formation in these objects (e.g. Morley et al. 2012).

The results of the 1D CARMA microphysical model from Gao et al. (2018), using the same input $T_{\text{eff}} = 400 \text{ K}$ and $\log g = 4.25$ but for a static atmosphere without feedback or dynamics, suggest a generally constant effective particle radius of $\sim 1 \mu\text{m}$ in the atmosphere. Due to the weak vertical velocities in the GCM, the main difference between our study and Gao et al. (2018) is the mixing rates, where Gao et al. (2018) consider stronger mixing rates of $K_{zz} = 10^6\text{-}10^8 \text{ cm}^2 \text{ s}^{-1}$. The $\log g = 5.25$, $K_{zz} = 10^6 \text{ cm}^2 \text{ s}^{-1}$ results in Gao et al. (2018) show the most similarity to our GCM results, especially the structure of the condensed mass and drop off in grain size to sub-micron with altitude from the cloud base. This qualitative similarity suggests our moment cloud method is adequately capturing the salient microphysical features of cloud formation process, qualitatively comparable to detailed bin models such as CARMA. However, more direct comparisons are required to make a more quantified assessment between the approaches.

5. Emission spectra and variability characteristics

We use the 3D radiative-transfer code, gCMCRT (Lee et al. 2022), to post-process the GCM simulation results. In Figure 4 we compare the emission spectra post-processes from the GCM to the JWST data in Beiler et al. (2023), who presented a wide wavelength JWST spectra of the Y-dwarf WISE J035934.06-540154.6 ($T_{\text{eff}} \approx 467 \text{ K}$), finding that models with weak mixing $K_{zz} \sim 10^4 \text{ cm}^2 \text{ s}^{-1}$ best reproduced the JWST spectral data. Our resultant spectra shows very little difference between post-processing with and without KCl cloud opacity, apart from shorter wavelengths, where some additional flux is present in spectral windows. This suggests that the KCl clouds have a minimal impact on the observational spectra, and T-p profile, characteristics of the atmosphere. Our GCM derived spectra is consistent with the WISE J035934.06-540154.6 data from Beiler et al. (2023) beyond $5 \mu\text{m}$ but is less consistent for shorter wavelength data. Our GCM produced NH_3 feature around $10\text{-}11 \mu\text{m}$ is also consistent with the data, as well as the longer wavelength infrared JWST photometric points. The smaller flux present at shorter wavelengths in the Beiler et al. (2023) data suggests that additional cloud opacity is present in WISE J035934.06-540154.6 compared to the GCM simulation.

Cushing et al. (2016) observed WISE J140518.39+553421.3 ($T_{\text{eff}} \approx 350\text{-}400 \text{ K}$, $P_{\text{rot}} \approx 8.5 \text{ hrs}$) with the Spitzer [3.6] and [4.5] bands, finding rotational variability of $\approx 3.5\%$. Leggett et al. (2016) observed WISEP J173835.52+273258.9 ($T_{\text{eff}} \approx 425 \text{ K}$, $P_{\text{rot}} \approx 6.0 \text{ hrs}$) using ground based and Spitzer photometry, finding variability on the order of $\approx 1.5\%$ in the [4.5] Spitzer band and $\sim 5\text{-}15\%$ in the Y band. Both the above studies note the need for 3D complex modelling to understand the origins of this variability. Figure 5 shows the Spitzer [3.6] and [4.5] bands relative flux curves from the GCM results. This shows small scale variability on the order of $\sim 0.2\%$, with no easily discernible rotational component. This suggests that the dynamical properties of our GCM combined with KCl clouds is not able to produce significant variability signatures in-line with the observational data. However, the relative flux density seems to be increasing

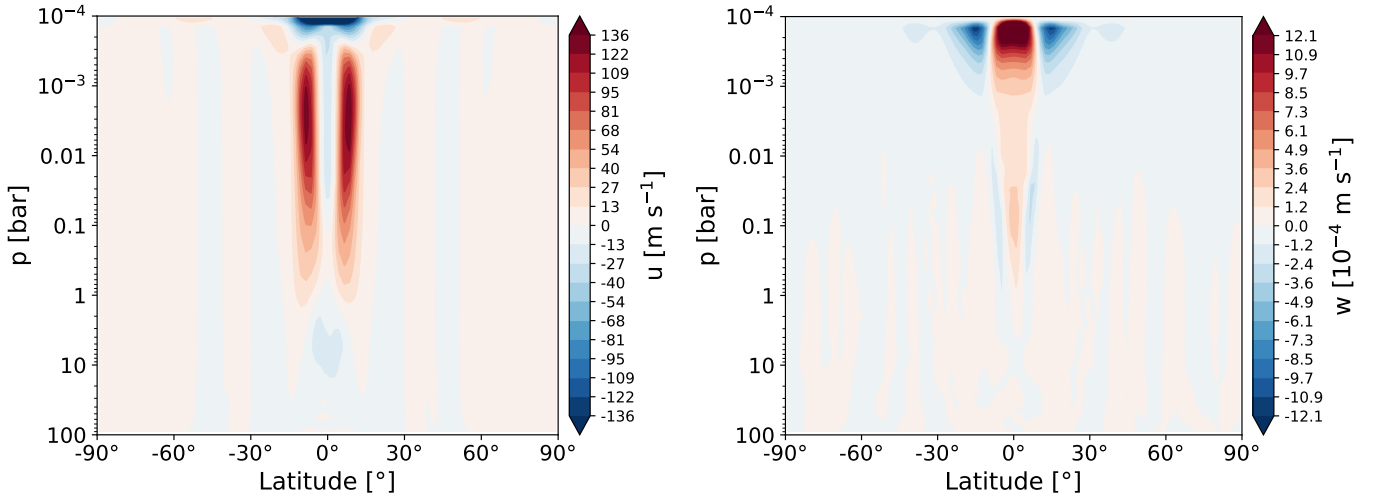


Fig. 1. Snapshot of the dynamical properties of the atmosphere after 500 days of simulation. Left: zonal mean zonal velocity. Right: zonal mean vertical velocity. Very little dynamical structure is present outside the equatorial region, leaving a generally sluggish and stagnant atmosphere.

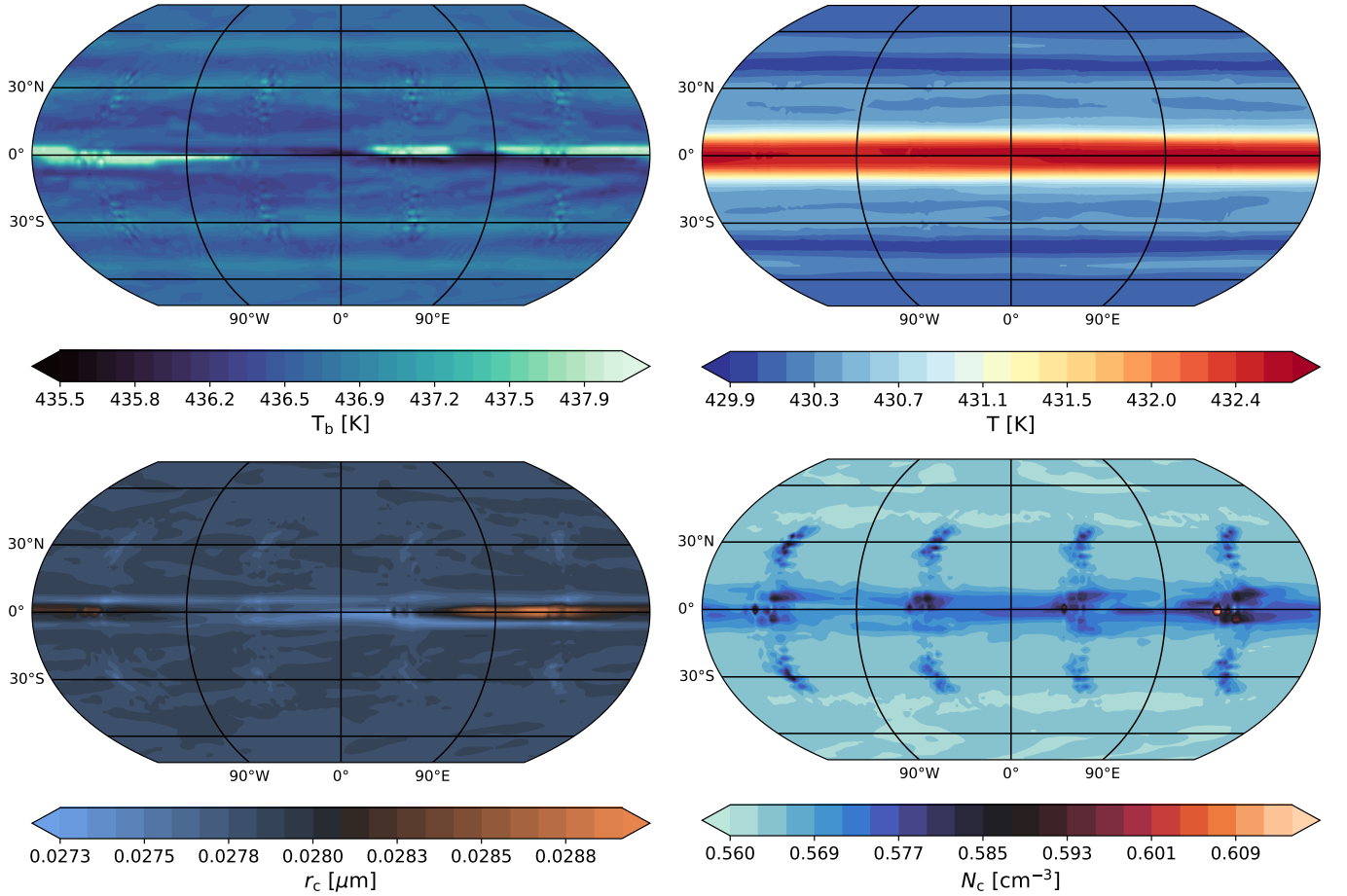


Fig. 2. Snapshot of the atmospheric conditions at 500 days of simulation. Top left: bolometric brightness temperature, T_b [K]. Top right: atmospheric temperature at the 0.3 bar pressure level. Bottom left: mass weighted average cloud particle size at the 0.3 bar pressure level. Bottom right: number density of the cloud particles at the 0.3 bar pressure level.

slowly with time, suggesting a longer dynamical pattern or thermal evolution present in the GCM simulation.

Our results suggest that for Y-dwarfs in our GCM dynamical regime, variability will be negligible due to KCl clouds. However, other clouds such as Na_2S , ZnS or NaCl may provide more cloud mass that can induce more variability signatures through

stronger impacts on the T-p profiles (e.g. Morley et al. 2012). Viewing angle is also an important consideration for characterising L/T dwarf atmospheres (e.g. Vos et al. 2017) and is likely to also play a critical role in explaining Y-dwarf variability. JWST Y-dwarf variability programs such as Skemer et al. (2021) will hopefully provide much needed insight into the chemical and

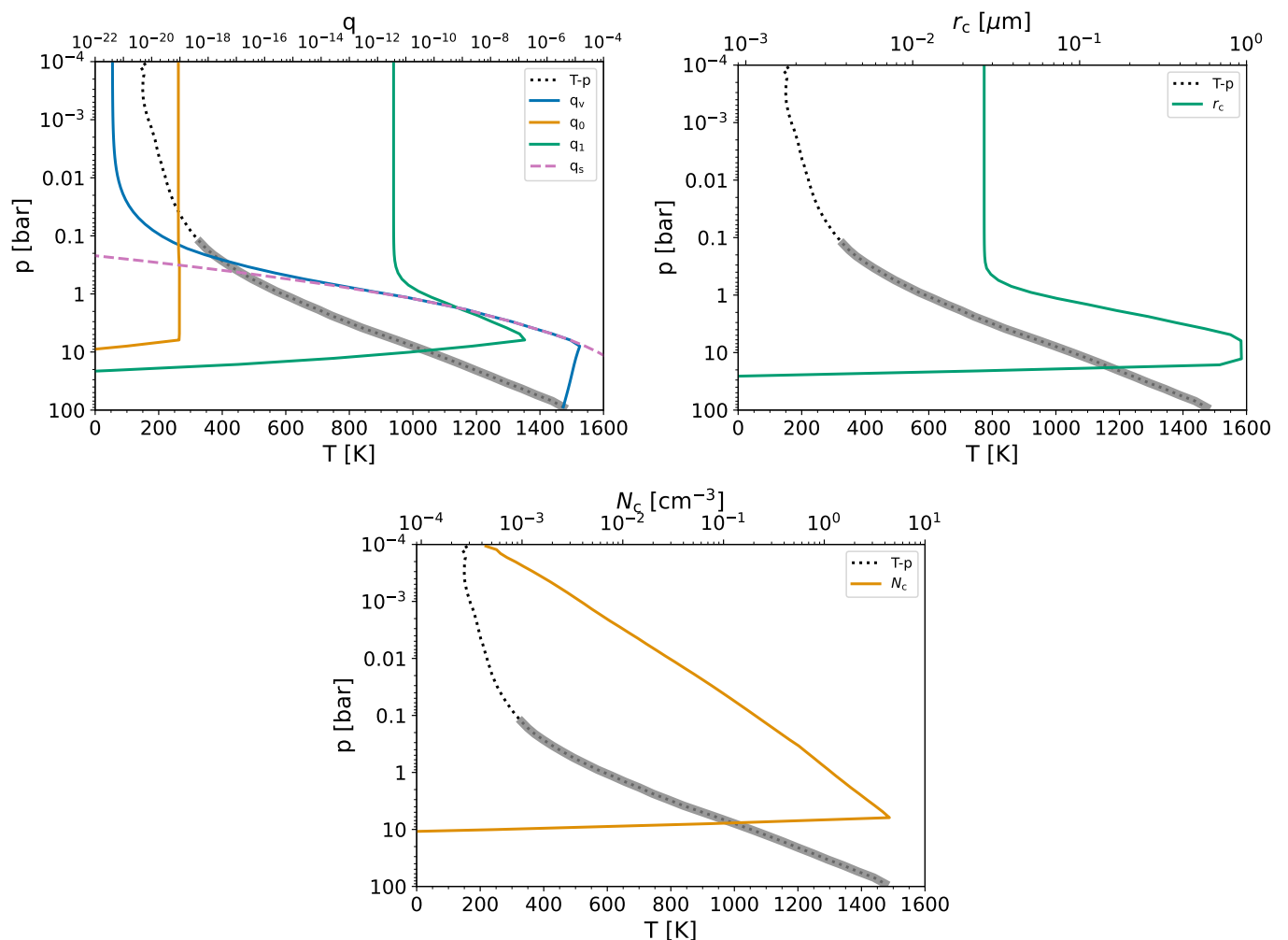


Fig. 3. Snapshot of the globally averaged properties of the GCM after 500 days of simulation. The dotted line shows the globally averaged T-p profile, with the grey shading denoting the convective region of the atmosphere. Top left: mixing ratio values for the moments and saturation mixing ratio (pink dashed line). Top right: mass weighted average cloud particle size. Bottom: number density of the cloud particles.

cloud variability through detailed time-dependent spectral information.

6. Discussion

Our results show that for our chosen dynamical regime, very weak mixing occurs, but small KCl particles $\sim 0.01 \mu\text{m}$ can remain lofted into the upper atmosphere. We therefore suggest that small KCl particles in the upper atmosphere of Y-dwarfs can provide surfaces for H_2O clouds to condense on efficiently, following a seed particle hierarchy discussed in Lee et al. (2018). Without this source of seed particles, H_2O clouds may struggle to form in Y-dwarfs above $T_{\text{eff}} \approx 350 \text{ K}$ due to the extra supersaturation required for self-nucleation of H_2O clouds (Lee et al. 2018). This mechanism is explored in detail by Mang et al. (2022) who show differences in the H_2O cloud profile when considering KCl seed particles or self- H_2O nucleation in this effective temperature range.

To estimate the dynamical regime of our GCM simulation, we compare qualitatively with the shallow water models performed in Hammond et al. (2023). The thermal timescale is approximately given by (e.g. Zhang & Showman 2014)

$$\tau_{\text{rad}} = \frac{p}{g} \frac{c_p}{4\sigma T_{\text{eff}}^3}, \quad (54)$$

with the non-dimensional radiative timescale given by $\Gamma = 2\Omega\tau_{\text{rad}}$. Assuming $p \approx 10^4 \text{ Pa}$ and $T_{\text{eff}} \approx 400 \text{ K}$, this gives $\tau_{\text{rad}} \approx 4.7 \cdot 10^4 \text{ s}$ and $\Gamma \approx 16$ for our simulation. Following Hammond et al. (2023), the thermal Rossby number for our simulation is $\text{Ro}_T \approx 6 \cdot 10^{-4}$. This places our simulation in the bottom left corner of the parameter space explored by Hammond et al. (2023) (their Figure 1.), which conforms to the general dynamical patterns found in our simulation of weak or no global jet or vortex features, with a stagnant atmosphere outside the equatorial region. However, weak jets are found near the equator where cloud coverage is thickest in our simulation, just above the cloud base (Fig. 1), suggesting that the KCl clouds are able to adequately force the appearance of weak dynamical jet features in the atmosphere. We suggest that these induced dynamical features would then be primarily responsible for the majority of the non-rotational component variability seen in these objects for this dynamical regime.

The current study does not include mixed or dirty grain compositions (e.g. Helling et al. 2008; Woitke et al. 2020), making the current model limited to single composition systems such as KCl. This can be included through modifying the moment equations in a similar manner to that considered in Helling et al. (2008) to take into account the condensation rate of different ma-

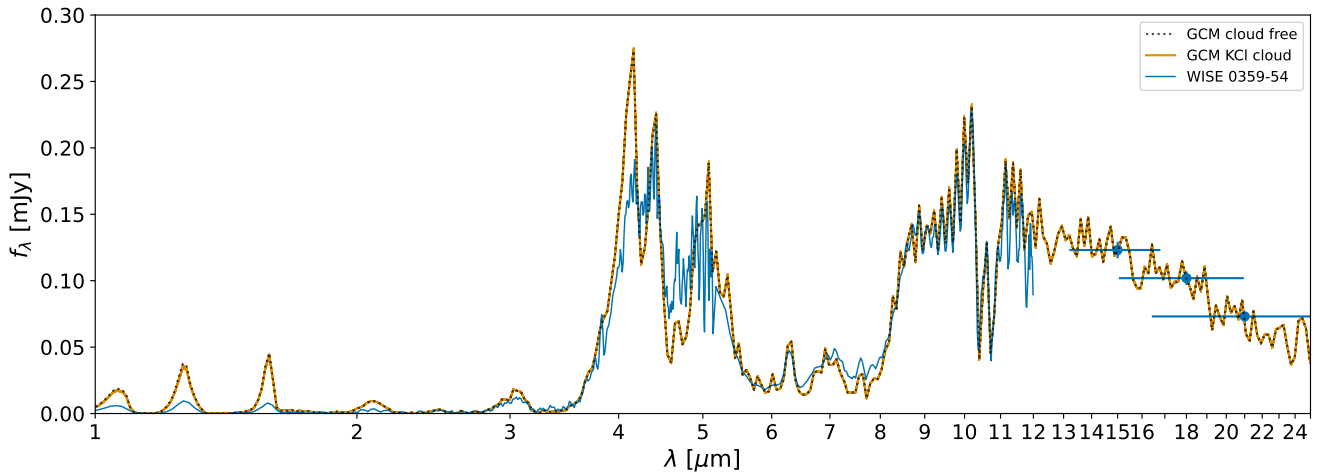


Fig. 4. Comparison between the post-processed spectra from the GCM and the WISE 0359-54 ($T_{\text{eff}} \approx 467$ K) JWST spectral data from Beiler et al. (2023). The GCM shows decent agreement beyond $10 \mu\text{m}$ but is not too consistent with the data at near-infrared wavelengths. The width of the orange line shows the extent of the maximum and minimum flux across the last 72 hours of simulation. The dotted black line shows the resultant spectra assuming no cloud opacity.

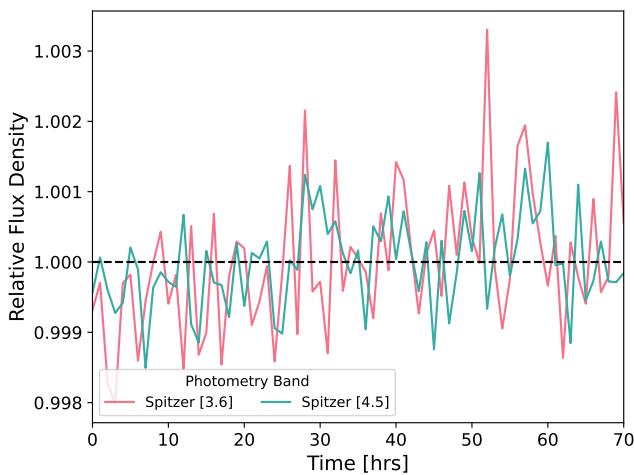


Fig. 5. Relative flux density for the Spitzer [3.6] and [4.5] bands produced from the last 72 hours of the GCM simulation. This shows minimal $\sim 0.2\%$ small scale variability with no discernible rotational component. The relative flux density is slowly increasing with time, suggesting a further long term evolution or dynamical cycle in the atmosphere.

terials onto the mixed grain surface. Mixed grain material in our mass moment framework will be examined in a follow up study.

In this study, we assumed a single particle size for deriving the settling velocity of the moments as well as the cloud opacity. This simplification enables efficient calculation, important for GCM simulations, but accuracy can be improved through assuming a particle size distribution derived from the values of the moments which may be more appropriate for detailed 1D modelling efforts using this method. In Appendix B we describe some relations using the moment results and deriving moment dependent vertical velocities and diffusion coupling, as well as integrating the particle size distribution to calculate opacities.

7. Conclusions

In this study, we present a 2-moment cloud bulk microphysical scheme for sub-stellar atmospheres that can be used for general time-dependent atmosphere simulations such as GCMs. Over-

all, our current model follows closely and combines the methods in Ohno & Okuzumi (2018) and Lee (2023) into a unified generalised bulk microphysical approach, combining homogeneous nucleation, condensation and collisional processes together.

In a test case, we simulated KCl cloud formation in a $T_{\text{int}} = 400$ K, $[\text{M}/\text{H}] = 0$, $\log g = 4.25$, $P_{\text{rot}} = 10$ hr Y-dwarf using the 3D Exo-FMS GCM coupled to the new 2-moment scheme. The GCM produces a generally sluggish and stagnant atmosphere, with near zero zonal and vertical velocities, especially outside the equatorial region. Compared to the weak jets expected from shallow water modelling (Hammond et al. 2023), our results suggest that the small thermal feedback from KCl clouds can help force the production of weak equatorial jets, on the order of Jupiter’s equatorial region ($\sim 100 \text{ m s}^{-1}$). Our GCM simulations show significant progress in modelling cold 3D brown dwarf atmospheres, including consistent chemistry, cloud microphysics and radiative-transfer, but several challenges and improvements with the current study remain to be resolved, such as grid imprinting error noise in such a stagnant atmosphere. More GCM studies in this parameter regime are warranted to understand the mechanisms of Y-dwarf variability more clearly.

Overall, the current 2-moment cloud microphysical scheme is highly suitable and computationally efficient enough for inclusion in large scale GCM simulations. The model can be extended to include ‘split’ moments, typically called ‘cloud’ and ‘rain’ components in Earth science literature (e.g. Seifert & Beheng 2001) similar to Ohno & Okuzumi (2017) as well as include mixed composition grains such as those considered in Helling et al. (2008). Latent heat, heterogeneous nucleation and surface Kelvin effects will also be explored in future iterations. The 2-moment schemes, as well as an implementation of the Komacek et al. (2022) saturation adjustment scheme are available online⁴.

Acknowledgements. E.K.H. Lee is supported by the CSH through the Bernoulli Fellowship. K. Ohno is supported by the JSPS KAKENHI Grant Number JP23K19072. This work benefited from the 2024 Exoplanet Summer Program in the Other Worlds Laboratory (OWL) at the University of California, Santa Cruz, a program funded by the Heising-Simons Foundation and NASA.

⁴ https://github.com/ELeeAstro/mini_cloud

References

- Ackerman, A. S. & Marley, M. S. 2001, *ApJ*, 556, 872
- Adams, D., Gao, P., de Pater, I., & Morley, C. V. 2019, *ApJ*, 874, 61
- Apai, D., Karalidi, T., Marley, M. S., et al. 2017, *Science*, 357, 683
- Beiler, S. A., Cushing, M. C., Kirkpatrick, J. D., et al. 2023, *ApJ*, 951, L48
- Bell, T. J., Crouzet, N., Cubillos, P. E., et al. 2024, *Nature Astronomy*, 8, 879
- Biller, B. A., Vos, J., Buenzli, E., et al. 2018, *AJ*, 155, 95
- Biller, B. A., Vos, J. M., Zhou, Y., et al. 2024, *MNRAS*, 532, 2207
- Bohren, C. F. & Huffman, D. R. 1983, *Absorption and scattering of light by small particles* (John Wiley & Sons)
- Bowler, B. P., Zhou, Y., Morley, C. V., et al. 2020, *ApJ*, 893, L30
- Brock, J. R. & Hidy, G. M. 1965, *Journal of Applied Physics*, 36, 1857
- Chandrasekhar, S. 1943, *Reviews of Modern Physics*, 15, 1
- Christie, D. A., Mayne, N. J., Lines, S., et al. 2021, *MNRAS*, 506, 4500
- Cushing, M. C., Hardegree-Ullman, K. K., Trucks, J. L., et al. 2016, *ApJ*, 823, 152
- Cushing, M. C., Roellig, T. L., Marley, M. S., et al. 2006, *ApJ*, 648, 614
- Cuzzi, J. N., Estrada, P. R., & Davis, S. S. 2014, *ApJS*, 210, 21
- Davidson, T. 1993, *A Simple and Accurate Method for Calculating Viscosity of Gaseous Mixtures*, Report of investigations (U.S. Department of the Interior, Bureau of Mines)
- Davies, C. N. 1945, *Proceedings of the Physical Society*, 57, 259
- Draine, B. T. & Salpeter, E. E. 1977, *J. Chem. Phys.*, 67, 2230
- Drake, R. L. 1972, *Journal of the Atmospheric Sciences*, 29, 537
- Dyrek, A., Min, M., Decin, L., et al. 2024, *Nature*, 625, 51
- Ehlers, K. & Moosmüller, H. 2023, *Aerosol Science Technology*, 57, 425
- Espinoza, N., Steinrueck, M. E., Kirk, J., et al. 2024, *Nature*
- Fuchs, N. 1964, *The Mechanics of Aerosols*, Dover books on engineering (Dover Publications)
- Gail, H. P., Keller, R., & Sedlmayr, E. 1984, *A&A*, 133, 320
- Gail, H.-P. & Sedlmayr, E. 2013, *Physics and Chemistry of Circumstellar Dust Shells*, Cambridge Astrophysics (Cambridge University Press)
- Gao, P. & Benneke, B. 2018, *ApJ*, 863, 165
- Gao, P., Marley, M. S., & Ackerman, A. S. 2018, *ApJ*, 855, 86
- Gao, P., Piette, A. A. A., Steinrueck, M. E., et al. 2023, *ApJ*, 951, 96
- Grant, D., Lewis, N. K., Wakeford, H. R., et al. 2023, *ApJ*, 956, L32
- Guillot, T., Ida, S., & Ormel, C. W. 2014, *A&A*, 572, A72
- Hammond, M., Mayne, N. J., Seviour, W. J. M., et al. 2023, *MNRAS*, 525, 150
- Hansen, J. E. 1971, *Journal of the Atmospheric Sciences*, 28, 1400
- Helling, C. & Fomins, A. 2013, *Philosophical Transactions of the Royal Society of London Series A*, 371, 20110581
- Helling, C., Woitke, P., & Thi, W. F. 2008, *A&A*, 485, 547
- Herning, F. & Zipperer, L. 1936, *Gas u. Wasserfach*, 79, 69
- Huang, H., Ormel, C. W., & Min, M. 2024, arXiv e-prints, arXiv:2409.18181
- Inglis, J., Batalha, N. E., Lewis, N. K., et al. 2024, *ApJ*, 973, L41
- Jacobson, M. Z. 2005, *Fundamentals of Atmospheric Modeling*, 2nd edn. (Cambridge University Press)
- Janz, G. J. 2013, *Molten salts handbook* (Elsevier)
- Kiefer, S., Gobrecht, D., Decin, L., & Helling, C. 2023, *A&A*, 671, A169
- Kitzmann, D. & Heng, K. 2018, *MNRAS*, 475, 94
- Komacek, T. D., Tan, X., Gao, P., & Lee, E. K. H. 2022, *ApJ*, 934, 79
- Lacy, B. & Burrows, A. 2023, *ApJ*, 950, 8
- Lavvas, P., Griffith, C. A., & Yelle, R. V. 2011, *Icarus*, 215, 732
- Lavvas, P., Yelle, R. V., & Griffith, C. A. 2010, *Icarus*, 210, 832
- Lee, E., Dobbs-Dixon, I., Helling, C., Bognar, K., & Woitke, P. 2016, *A&A*, 594, A48
- Lee, E. K. H. 2023, *MNRAS*, 524, 2918
- Lee, E. K. H., Blecic, J., & Helling, C. 2018, *A&A*, 614, A126
- Lee, E. K. H., Parmentier, V., Hammond, M., et al. 2021, *MNRAS*, 506, 2695
- Lee, E. K. H., Tan, X., & Tsai, S.-M. 2023, *MNRAS*, 523, 4477
- Lee, E. K. H., Tan, X., & Tsai, S.-M. 2024, *MNRAS*, 529, 2686
- Lee, E. K. H., Wardenier, J. P., Prinoth, B., et al. 2022, *ApJ*, 929, 180
- Leggett, S. K., Cushing, M. C., Hardegree-Ullman, K. K., et al. 2016, *ApJ*, 830, 141
- Lines, S., Mayne, N. J., Boutle, I. A., et al. 2018, *A&A*, 615, A97
- Lines, S., Mayne, N. J., Manners, J., et al. 2019, *MNRAS*, 488, 1332
- Looper, D. L., Kirkpatrick, J. D., Cutri, R. M., et al. 2008, *ApJ*, 686, 528
- Luna, J. L. & Morley, C. V. 2021, *ApJ*, 920, 146
- Mang, J., Gao, P., Hood, C. E., et al. 2022, *ApJ*, 927, 184
- Metchev, S. A., Heinze, A., Apai, D., et al. 2015, *ApJ*, 799, 154
- Miles, B. E., Biller, B. A., Patapis, P., et al. 2023, *ApJ*, 946, L6
- Moosmüller, H. & Sorensen, C. M. 2018, *J. Quant. Spectr. Rad. Transf.*, 219, 333
- Moran, S. E., Marley, M. S., & Crossley, S. D. 2024, *The Astrophysical Journal Letters*, 973, L3
- Morley, C. V., Fortney, J. J., Marley, M. S., et al. 2012, *ApJ*, 756, 172
- Morley, C. V., Marley, M. S., Fortney, J. J., & Lupu, R. 2014, *ApJ*, 789, L14
- Morrison, H., van Lier-Walqui, M., Fridlind, A. M., et al. 2020, *Journal of Advances in Modeling Earth Systems*, 12, e2019MS001689, e2019MS001689
- Müller, H. 1928, *Kolloidchemische Beihefte*, 27, 223
- Murphy, M. M., Beatty, T. G., Schlawin, E., et al. 2024, *Nature Astronomy*
- Ohno, K. 2024, arXiv e-prints, arXiv:2410.10197
- Ohno, K. & Okuzumi, S. 2017, *ApJ*, 835, 261
- Ohno, K. & Okuzumi, S. 2018, *ApJ*, 859, 34
- Ohno, K., Okuzumi, S., & Tazaki, R. 2020, *ApJ*, 891, 131
- Ormel, C. W. & Min, M. 2019, *A&A*, 622, A121
- Palik, E. D. 1985, *Handbook of optical constants of solids* (Academic Press)
- Parmentier, V., Fortney, J. J., Showman, A. P., Morley, C., & Marley, M. S. 2016, *ApJ*, 828, 22
- Porco, C. C., West, R. A., McEwen, A., et al. 2003, *Science*, 299, 1541
- Powell, D., Loudon, T., Kreidberg, L., et al. 2019, *ApJ*, 887, 170
- Powell, D. & Zhang, X. 2024, *ApJ*, 969, 5
- Pruppacher, H. R. & Klett, J. D. 1978, *Microphysics of Clouds and Precipitation* (Springer Dordrecht)
- Putman, W. M. & Lin, S.-J. 2007, *Journal of Computational Physics*, 227, 55
- Querry, M. 1987, Contractor rept. Jun 1985-May 1987
- Radhakrishnan, K. & Hindmarsh, A. C. 1993, Description and use of LSODE, the Livermore solver for ordinary differential equations, Tech. Rep. UCLRL-ID-113855, Lawrence Livermore National Laboratory
- Radigan, J., Lafrenière, D., Jayawardhana, R., & Artigau, E. 2014, *ApJ*, 793, 75
- Robinson, T. D. & Marley, M. S. 2014, *ApJ*, 785, 158
- Rooney, C. M., Batalha, N. E., & Marley, M. S. 2024, *ApJ*, 960, 131
- Rosner, D. E. 2012, Transport processes in chemically reacting flow systems (Courier Corporation)
- Rosow, W. B. 1978, *Icarus*, 36, 1
- Samra, D., Helling, C., & Birnstiel, T. 2022, *A&A*, 663, A47
- Sato, T., Okuzumi, S., & Ida, S. 2016, *A&A*, 589, A15
- Schlawin, E., Mukherjee, S., Ohno, K., et al. 2024, *AJ*, 168, 104
- Schonenberg Ferrier, B. 1994, *Journal of the Atmospheric Sciences*, 51, 249
- Seifert, A. & Beheng, K. D. 2001, *Atmospheric Research*, 59, 265
- Showman, A. P., Tan, X., & Zhang, X. 2019, *ApJ*, 883, 4
- Sindel, J. P., Gobrecht, D., Helling, C., & Decin, L. 2022, *A&A*, 668, A35
- Skemer, A., Miles, B. E., Morley, C., et al. 2021, *Water Ice Clouds and Weather on the Coldest Brown Dwarf*, JWST Proposal. Cycle 1, ID. #2327
- Smoluchowski, M. V. 1916, *Zeitschrift für Physik*, 17, 557
- Suárez, G. & Metchev, S. 2022, *MNRAS*, 513, 5701
- Tan, X. & Showman, A. P. 2019, *ApJ*, 874, 111
- Tan, X. & Showman, A. P. 2021, *MNRAS*, 502, 2198
- Teinturier, L., Charnay, B., Spiga, A., et al. 2024, *A&A*, 683, A231
- Toon, O. B., McKay, C. P., Ackerman, T. P., & Santhanam, K. 1989a, *J. Geophys. Res.*, 94, 16287
- Toon, O. B., Turco, R. P., Jordan, J., Goodman, J., & Ferry, G. 1989b, *J. Geophys. Res.*, 94, 11,359
- Tremblin, P., Phillips, M. W., Emery, A., et al. 2020, *A&A*, 643, A23
- Tsai, S.-M., Lee, E. K. H., & Pierrehumbert, R. 2022, *A&A*, 664, A82
- Vincenti, W. & Kruger, C. 1965, *Introduction to Physical Gas Dynamics* (Wiley)
- Vos, J. M., Allers, K. N., & Biller, B. A. 2017, *ApJ*, 842, 78
- Vos, J. M., Biller, B. A., Bonavita, M., et al. 2019, *MNRAS*, 483, 480
- Wakeford, H. R. & Sing, D. K. 2015, *A&A*, 573, A122
- Wilke, C. R. 1950, *Journal of Chemical Physics*, 18, 517
- Woitke, P. & Helling, C. 2003, *A&A*, 399, 297
- Woitke, P., Helling, C., & Gunn, O. 2020, *A&A*, 634, A23
- Woitke, P., Helling, C., Hunter, G. H., et al. 2018, *A&A*, 614, A1
- Yang, H., Apai, D., Marley, M. S., et al. 2015, *ApJ*, 798, L13
- Zhang, X. & Showman, A. P. 2014, *ApJ*, 788, L6
- Zhou, Y., Bowler, B. P., Morley, C. V., et al. 2020, *AJ*, 160, 77
- Ziegler, C. L. 1985, *Journal of the Atmospheric Sciences*, 42, 1487

Appendix A: Full derivation of the moment equations

In general, one can describe the evolution of particle size distribution as

$$\begin{aligned} \frac{\partial f(m)}{\partial t} = & -\nabla \cdot (\mathbf{V}_{\text{wind}} f(m)) - \frac{\partial [v_f(m) f(m)]}{\partial z} - \frac{\partial}{\partial m} \left[\left(\frac{dm}{dt} \right)_{\text{cond}} f(m) \right] \\ & + \frac{1}{2} \int_0^{m-m'} K(m', m-m') f(m') f(m-m') dm' \\ & - f(m) \int_0^\infty K(m, m') f(m') dm' + J(m), \end{aligned} \quad (\text{A.1})$$

where \mathbf{V}_{wind} is the 3D velocity vector of atmospheric wind, $J(m)$ is the nucleation rate of particles with a mass of m . In the right side, the first and the second terms stand for spatial advection due to atmospheric flow and particle's gravitational settling, the third term stands for the advection in a mass space driven by condensation or evaporation, the fourth and the fifth terms express the gain and loss of cloud particles through collisional sticking, and the sixth term expresses the new particle formation through nucleation. Multiplying m^k and integrating the equation over whole mass space, we obtain

$$\begin{aligned} \frac{\partial M^{(k)}}{\partial t} = & -\nabla \cdot (\mathbf{V}_{\text{wind}} M^{(k)}) - \frac{\partial (\bar{v}_f^{(k)} M^{(k)})}{\partial z} \\ & + m_{\text{seed}}^k J_{\text{hom}} + \int_0^\infty k m^{k-1} \left(\frac{dm}{dt} \right)_{\text{cond}} f(m) dm \\ & + \frac{1}{2} \int_0^\infty \int_0^\infty [(m+m')^k - m^k - m'^k] \\ & \quad \times K(m', m) f(m') f(m) dm dm', \end{aligned} \quad (\text{A.2})$$

where we have used the conversion of collision term given by Equation (13) and assumed that $(dm/dt)f(m)$ converges to zero at $m \rightarrow 0$ and $m \rightarrow \infty$. The averaged terminal velocity \bar{v}_f is defined as

$$\bar{v}_f^{(k)} = \frac{\int_0^\infty m^k v_f(m) f(m) dm}{\int_0^\infty m^k f(m) dm}. \quad (\text{A.3})$$

We also express the homogeneous nucleation rate profile as $J(m) = J_{\text{hom}} \delta(m - m_{\text{seed}})$, where $\delta(x)$ is the delta function.

For the zeroth ($k = 0$) and first moment ($k = 1$), one can simplify Equation (A.2) as

$$\begin{aligned} \frac{\partial M^{(0)}}{\partial t} = & -\nabla \cdot (\mathbf{V}_{\text{wind}} M^{(0)}) - \frac{\partial (\bar{v}_f^{(0)} M^{(0)})}{\partial z} \\ & + J_{\text{hom}} - \frac{1}{2} \int_0^\infty \int_0^\infty K(m', m) f(m') f(m) dm dm', \end{aligned} \quad (\text{A.4})$$

$$\begin{aligned} \frac{\partial M^{(1)}}{\partial t} = & -\nabla \cdot (\mathbf{V}_{\text{wind}} M^{(1)}) - \frac{\partial (\bar{v}_f^{(1)} M^{(1)})}{\partial z} \\ & + m_{\text{seed}} J_{\text{hom}} + \int_0^\infty \left(\frac{dm}{dt} \right)_{\text{cond}} f(m) dm. \end{aligned} \quad (\text{A.5})$$

These simplification reflect the fact that condensation does not change the total particle number ($N_c = M^{(0)}$), whereas collision does not change the total particle mass ($\rho_c = M^{(1)}$) regardless of the expression of the size distribution, the condensation rate, and the collision Kernel.

Appendix A.1: 2-moment model

To move forward from Equation (A.2), one needs to assume a certain shape of the size distribution $f(m)$ to obtain explicit expressions of each source term. The simplest size distribution is the delta function $f(m) = N_c \delta(m - m_c)$, meaning that cloud particles at each vertical layer are characterized by a single particle size (mass). This approach has been widely used in the models of grain growth in protoplanetary disks (e.g., Sato et al. 2016). Since the assumed size distribution contains 2 unknowns, N_c and m_c , two moments are needed to close the system. Each moment is related to N_c and m_c as

$$M^{(0)} = N_c \quad (\text{A.6})$$

$$M^{(1)} = \rho_c = m_c N_c \quad (\text{A.7})$$

Inserting $f(m) = N_c \delta(m - m_c)$ into Equation (A.2), we obtain the master equation of the 2-moment model:

$$\frac{\partial N_c}{\partial t} = -\nabla \cdot (\mathbf{V}_{\text{wind}} N_c) - \frac{\partial (v_f(m_c) N_c)}{\partial z} + J_{\text{hom}} - \frac{1}{2} K(m_c, m_c) N_c^2, \quad (\text{A.8})$$

$$\frac{\partial \rho_c}{\partial t} = -\nabla \cdot (\mathbf{V}_{\text{wind}} \rho_c) - \frac{\partial (v_f(m_c) \rho_c)}{\partial z} + m_{\text{seed}} J_{\text{hom}} + N_c \left(\frac{dm}{dt} \right)_{\text{cond}, m=m_c}. \quad (\text{A.9})$$

These expressions are equivalent to the model of Ohno & Okuzumi (2018), though they approximated the wind transport by eddy diffusion for 1D framework and omitted homogeneous nucleation. We note that the approximation of $f(m) = N_c \delta(m - m_c)$ leads to the same moment-averaged terminal velocity for zeroth and first moment, i.e., $\bar{v}_f^{(0)} = \bar{v}_f^{(1)} = v_f(m_c)$.

The 2-moment framework has been extensively utilized in the microphysical model of Earth clouds (for review, see e.g., Morrison et al. 2020). We note that 2 moment framework does not necessary need to assume the delta function for the size distribution. For instance, 2-moment models for Earth cloud often assume a gamma distribution (e.g., Ziegler 1985; Schoenberg Ferrier 1994), given by

$$f(m) = \frac{N_c \beta^{\alpha+1}}{\Gamma(\alpha+1)} m^\alpha \exp(-\beta m), \quad (\text{A.10})$$

where $\Gamma(x) \equiv \int_0^\infty y^{x-1} e^{-y} dy$ is the gamma function. The gamma distribution includes 3 unknown parameters (N_c , α , β), which require three moments to close the system. However, one could reduce the number of unknowns by treating one of them as a free parameter, which allows us to use the gamma distribution for 2-moment framework (α is typically fixed in Earth cloud models, Ziegler 1985; Schoenberg Ferrier 1994). This approach can be useful if existing observations have already put constraint on the shape of size distribution, as in the cases of Earth clouds. On the other hand, the shape of particle size distributions remain highly uncertain for brown dwarf and exoplanetary atmospheres. Thus, we decided to keep adopting the simple delta function derivation for the present 2-moment model, as in Ohno & Okuzumi (2018).

Appendix B: Size distribution effects

In this Appendix, we detail fitting particle mass and size distributions from the results of the moment equations. We also show distribution integrated cloud opacities using the fit distributions.

Appendix B.1: Fitting mass and size distributions

Deriving continuous size distributions from the moment solutions is first performed by deriving the expectation value $E[m]$ [g] (mean value) and variance $V[m]$ [g²] of the mass distribution. These are given by

$$E[m] = \frac{\rho_c}{N_c}, \quad (\text{B.1})$$

and

$$V[m] = \frac{Z_c}{N_c} - \left(\frac{\rho_c}{N_c}\right)^2. \quad (\text{B.2})$$

In these examples, for simplicity we assume a particle density of $\rho_d = 1 \text{ g cm}^{-3}$, the total number density is $N_c = 1 \text{ cm}^{-3}$, the mass expectation value (mean) $E[m] = 10^{-11} \text{ g}$ and particle size variance $V[m] = 10^{-11} \text{ g}^2$. In Figure B.1 we show each of the derived distributions in mass and radius space.

The mass grid, m [g], is converted to a radius grid, r [cm], assuming spherical particles from the relation

$$m = \frac{4}{3}\pi r^3 \rho_d. \quad (\text{B.3})$$

The mass particle size distribution, $f(m)$ [cm⁻³ g⁻¹], is converted to the particle radius distribution, $f(r)$ [cm⁻³ cm⁻¹], through the relation

$$f(r) = \frac{3mf(m)}{r}, \quad (\text{B.4})$$

where the factor of 3 is required to recover the correct integrated values of the distribution. Therefore, we can use the mass moments to fit a particle mass distribution, then convert it to a radius distribution to facilitate calculations. For the log-normal distribution, the median particle mass, m_m [g] and standard deviation, σ [g] are derived from the expectation value and variance from

$$\sigma = \exp \left[\sqrt{\ln \left(1 + \frac{V[m]^2}{E[m]^2} \right)} \right], \quad (\text{B.5})$$

and

$$m_m = \frac{E[m]}{\exp[\ln(\sigma^2)]}. \quad (\text{B.6})$$

The particle mass distribution is then

$$f(m) = \frac{N_c}{m\sigma\sqrt{2\pi}} \exp \left[-\frac{(\ln m - \ln m_m)^2}{2\sigma^2} \right]. \quad (\text{B.7})$$

The inverse gamma distribution is given through first driving the α and β parameters

$$\alpha = \frac{E[m]^2}{V[m]} + 2, \quad (\text{B.8})$$

$$\beta = E[m](\alpha - 1). \quad (\text{B.9})$$

The mass distribution is then

$$f(m) = \frac{N_c \beta^\alpha}{\Gamma(\alpha)} \left(\frac{1}{m}\right)^{\alpha+1} \exp(-\beta/m). \quad (\text{B.10})$$

The exponential distribution is a single parameter distribution given by the λ parameter

$$\lambda = \frac{1}{E[m]}, \quad (\text{B.11})$$

with the distribution given by

$$f(m) = N_c \lambda \exp(-\lambda m). \quad (\text{B.12})$$

The exponential distribution is useful for consideration when using the 2-moment scheme as only the expectation value is required to estimate the λ parameter.

The Rayleigh distribution is another single parameter distribution given by the σ value

$$\sigma = \frac{E[m]}{\sqrt{\pi/2}}, \quad (\text{B.13})$$

where the distribution as

$$f(m) = \frac{N_c}{\sigma^2} \exp\left(-\frac{m^2}{2\sigma^2}\right). \quad (\text{B.14})$$

As with the exponential distribution, as a single parameter distribution, the Rayleigh distribution is also useful to consider for 2-moment schemes.

We note, that in our current scheme it is not possible (without approximation) to estimate other particle size distributions that require higher moment powers such as the potential exponential in [Helling et al. \(2008\)](#) and the Hansen distribution ([Hansen 1971](#)).

Appendix B.2: Distribution integrated opacity

To calculate the extinction opacity, single scattering albedos and asymmetry factor from the particle mass distribution, the particle radius distribution must be first calculated as in the previous sections. Typically, the area weighted radius, known as the effective radius, r_{eff} [cm], can be used as a representative value to calculate the opacity. If the particle size distribution is well peaked, then $r_{\text{eff}} \approx r_c$ and Eq. 5 can be used in the opacity calculation. However, if the distribution is broad, then the effective radius can be usually calculated from considering the shape of the distribution function. For example, if the distribution is log-normal, the effective radius is related to the mass weighted radius from

$$r_{\text{eff}} = r_c \exp\left[-\ln(\sigma^2)\right]. \quad (\text{B.15})$$

To calculate the distribution integrated quantities self-consistently, the following equations are used for the extinction opacity, $\bar{\kappa}_{\text{ext}}$ [cm² g⁻¹],

$$\bar{\kappa}_{\text{ext}} = \frac{1}{\rho_a} \int_0^\infty \pi r^2 Q_{\text{ext}}(r) f(r) dr, \quad (\text{B.16})$$

the single scattering albedo, $\bar{\omega}$,

$$\bar{\omega} = \frac{\int_0^\infty \pi r^2 Q_{\text{sca}}(r) f(r) dr}{\int_0^\infty \pi r^2 Q_{\text{ext}}(r) f(r) dr}, \quad (\text{B.17})$$

and asymmetry factor, \bar{g} ,

$$\bar{g} = \frac{\int_0^\infty \pi r^2 Q_{\text{sca}}(r) g(r) f(r) dr}{\int_0^\infty \pi r^2 Q_{\text{sca}}(r) f(r) dr}. \quad (\text{B.18})$$

The extinction and scattering efficiency factors $Q_{\text{ext}}(r)$ and $Q_{\text{sca}}(r)$ as well as the radius dependent asymmetry factor $g(r)$ can be calculated using Mie theory, approximations to Mie theory or other methods.

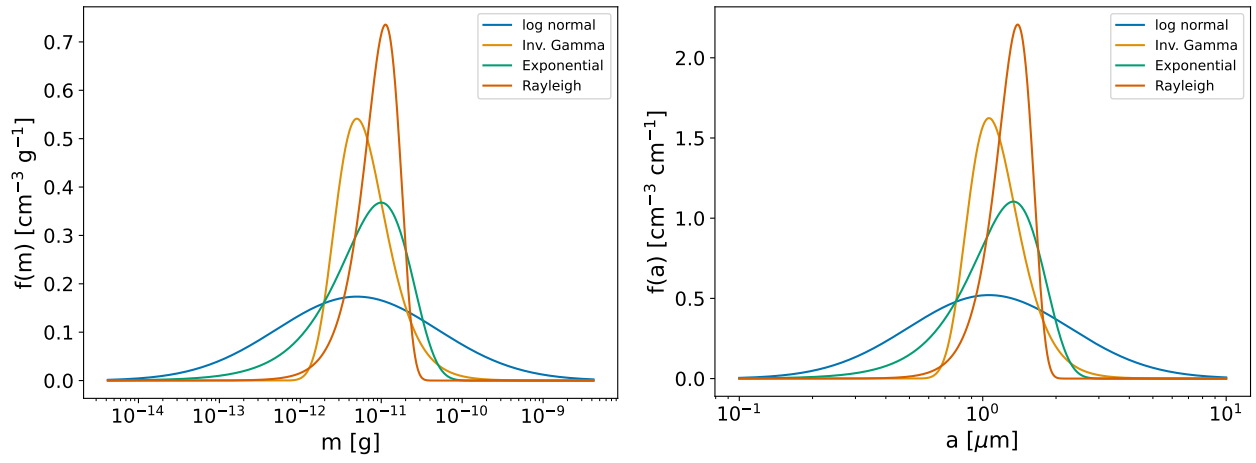


Fig. B.1. Particle mass distribution (left) and equivalent particle radius distribution (right). The difference in magnitude scale between the two is large, with the mass distributed over many more magnitudes compared to the radius.